CIBA

Configurable Interferometer Baseline Array

A Proposed Design Prototype for a New Generation of Astronomical Interferometer

A Thesis submitted in Partial Satisfaction

Of the Requirements for the Degree of

Bachelor of Sciences in Astrophysics

at the

University of California, Santa Cruz

By

Charles K. Lundquist

8-26-2010

Rachel Dewey Advisor	David P. Belanger Senior Thesis Coordinator

David P. Belanger
Chair, Department of Physics

This proposed design prototype for a short-baseline optical astronomical interferometer provides superior UV-plane coverage and yet is cost-effective. This enhanced UV-plane coverage is achieved by employing variable baseline lengths and variable baseline orientations, which allow for increased detector integration times and fixed/reproducible interferometer baseline orientations. By synthesizing existing technologies, materials, and techniques it is feasible to construct an astronomical interferometer capable of viable scientific research for minimal costs for construction, maintenance, as well as upgrades.

Table of Contents

Abstract 2
Table of Contents 3
I Introduction 4
II Image Resolution and Fourier Transform Optics 6
  Point Spread Function (PSF) and Fourier Transform Optics 6
  Two Aperture Interference 10
  Resolution 12
III Instrument Measurements and Design Considerations 17
  Visibility 17
  Baselines and Optical Path Length 18
  Design Considerations 20
IV Proposed Design Overview 21
  Array Mount and Drive 21
  Array Platform and Drive 22
  Optical System 24
  Cost Effectiveness 26
Bibliography and References 27

I Introduction

The field of astronomical interferometry at optical wavelengths has proven to be technically challenging, though modern instruments, along with maturing technologies and manufacturing processes, have propelled this field to the forefront of observational astronomy. The vast majority of current instruments are grand in scale and continue to extend the capabilities of researchers. And in observational astronomy, bigger IS better. However, bigger is also more costly, and generally prohibitively so, whereas adequate may also be affordable. The intersection between resolving power and affordability is the short-baseline optical interferometer.

Interferometers offer substantially enhanced resolving power over a single aperture instrument, on the order of a single instrument with a primary objective diameter comparable to the baseline of the interferometer. Although interferometers offer enhanced resolution they are limited in light grasp, which is a function of the surface area of the apertures rather than separation of the apertures. Long baseline interferometers inherently have technical challenges that are daunting, yet a short baseline interferometer can circumvent some of these issues simplifying the technical considerations required for this proposed design.

Functionality and cost are the two primary concerns with this design, the key features of this proposed design include:

- Inexpensive construction costs
- Low maintenance cost
- Low operating cost
- High angular resolution
- Variable baseline length
- Variable baseline orientation
- Readily upgradeable

In terms of functionality, the instrument should be versatile and capable of conducting viable research now and in the future. Some of the potential avenues of research for this instrument include:

- Active galactic nuclei (AGN)
- Star formation
- Stellar accretion and mass-loss
- Photospheric diameters
- Stellar limb darkening
- Stellar surface structure
- Observations of low-mass companions (such as HD209458)[1]

[1] HD209458 has a low-mass companion that can be detected with an 8' telescope and a CCD camera by measuring the intensity variations as the planet transits the star (2).

This paper will lay out a prototype design for a new generation of astronomical optical interferometer. By synthesizing existing technologies and materials into a highly flexible and cost-effective system, it's possible to propose a prototype design for a configurable interferometer baseline array. The key feature of this design is the ability to orient the baseline of the interferometer in the desired direction, allowing maximum resolution of the object in the desired direction. A close view of the proposed design will offer better insight into the functionality and cost effectiveness of the system, and a detailed examination follows.

We will examine what a typical interferometer measures and identify the major components of current designs that affect these measurements. This will be followed by an overview of the proposed design introducing the major subsystems of the interferometer, as well as a detailed examination of these subsystems. But first we will examine the influence of the optical system on incident wave fronts and how this translates to the observed image and the resolving power of the instrument.

II Image Resolution and Fourier Transform Optics

When observing a distant point source through a telescope the resulting image is never a point whether one is observing visually, with film, or with a CCD, but rather the resulting point is blurred out over a small area. This effect is can be mathematically modeled and is known as the Point Spread Function (PSF) of the system. In this chapter we examine this effect and its influence on the resolving power of an optical system, and will consider only the simplest cases where the aperture plane is a surface with a hole in it and the image plane as a screen or wall behind, and parallel with, the aperture pane. The actual PSF of a given optical system is far more complicated due to the geometry of the instrument, compression of the field at the image plane, and imperfections in the system. We will examine the resolving power of 3 specific examples, which include a single 0.25m aperture, a single 10m aperture, and a pair of 0.25m apertures. But first we need to calculate the PSF for a single circular aperture as well as the PSF for a pair of circular apertures.

Point Spread Function (PSF) and Fourier Transform Optics

What we seek is the normalized intensity distribution of the incoming wave-front at the image plane due to the response of the wave-front at the aperture plane, which is known as the point spread function, or PSF. To analyze the response of an aperture to the incoming wave-front we will examine the specific case of a 2-dimensional circular aperture of radius a. We will assume a monochromatic point source located at infinity, and therefore the incoming wave-front can be treated as a plane-wave. Furthermore we define the central-axis as the axis that is normal to the center of the aperture, hence the z-axis in Fig. 2.1 below is the central-axis of the aperture.

First we consider a one dimensional aperture of length $2a$. We define the transmission function of the aperture as the fraction of incident radiation which is transmitted:

$$T(x) = \begin{cases} 1 & -a \le x \le a \\ 0 & |x| > a \end{cases} \qquad \textbf{Eqn. 2.1}$$

The intensity, per unit length of aperture, of the electric field E, where c is the speed of light and ε_0 is the permittivity of free space, is given by:

$$I \equiv \langle \mathbf{S} \rangle = \frac{1}{2} c \varepsilon_0 E_o^2 \qquad \text{(3, pp. 381 eq. 9.63)}$$

The equation for the complex electric field of a monochromatic plane wave is given by $\tilde{\mathbf{E}}(\mathbf{r},t) = \tilde{\mathbf{E}}_0 e^{i(k\mathbf{r}-\omega t)}\hat{\mathbf{n}}$ (3, pp. 379). Given that we are seeking the intensity, which is proportional to the time average of the electric field squared, we can neglect the temporal components. From Fig. 2.1 (below) we see that the electric field for an incident plane wave and for the transmitted wave we have:

$$\tilde{\mathbf{E}}_I(z) = \tilde{\mathbf{E}}_I e^{ikz}.$$

$$\tilde{\mathbf{E}}_T(r) = \tilde{\mathbf{E}}_T e^{ikr} = \tilde{\mathbf{E}}_T e^{ikx\sin\theta}$$

For a point source coincident with the central-axis, the contribution to the electric field at angle of θ from the central-axis, through an element dx of the aperture, is proportional to $T(x)e^{ikx\sin\theta}$, and the total electric field at an angle θ is proportional to:

$$U(\theta) \propto \int_{-\infty}^{\infty} T(x)e^{ikx\sin\theta}dx.$$

Here we should recognize that the resulting electric field is the Fourier transform of the transmission function: $f(y) = \int_{-\infty}^{\infty} g(x)e^{ixy}\,dx$ (4, pp. 648).

To find the normalized intensity on the image plane, at angle of θ from the central axis, we note that the intensity is proportional to the square of the total energy at that point. Also, at optical wavelengths the aperture diameter is much greater than the length of the incoming wave minimizing the effects of diffraction allowing us to use the small angle approximation $\sin(\theta) \approx \theta$. This leads us to:

$$I(\theta) \propto [U(\theta)]^2 \propto \left[\int_{-\infty}^{\infty} T(x)e^{ikx\sin\theta}dx\right]^2 = \left[\int_{-\infty}^{\infty} T(x)e^{ikx\theta}dx\right]^2$$

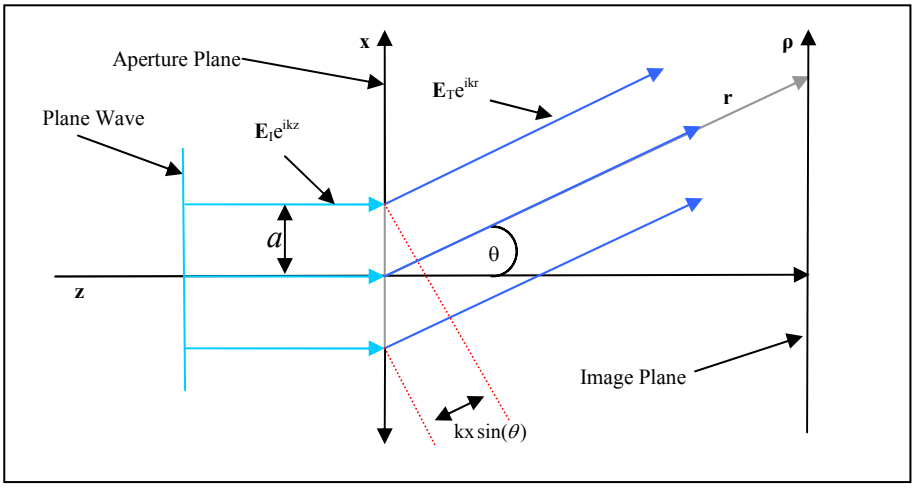

Figure 2.1 Electric Field of Incident Wave

Next we extend this to a 2-dimensional plane, in the direction of y in the aperture plane, and the direction of ϕ in the image plane. Combining this with the electric field in the x-direction:

$$U(\theta,\phi) \propto \int_{-\infty}^{\infty}\int_{-\infty}^{\infty} T(x,y)e^{ikx\theta}e^{iky\phi}dxdy = \int_{-\infty}^{\infty}\int_{-\infty}^{\infty} T(x,y)e^{ik(x\theta+y\phi)}dxdy$$

Now we can cast this expression into polar coordinates for a circular aperture of radius a. We need to redefine the transmission function for a circular aperture:

$$T(r)=\begin{cases}1 & 0\le r\le a\\ 0 & r>a\end{cases}$$

From Fig. 2.2 (below) we see that we wish to recast the aperture coordinates from x,y Cartesian coordinates to r,α polar coordinates, giving us:

$$x=r\cos\alpha \text{ and } y=r\sin\alpha$$

And for the image plane from θ,ϕ cartesian coordinates to ρ,β polar coordinates,

$$\theta=\rho\cos\beta \text{ and } \phi=\rho\sin\beta$$

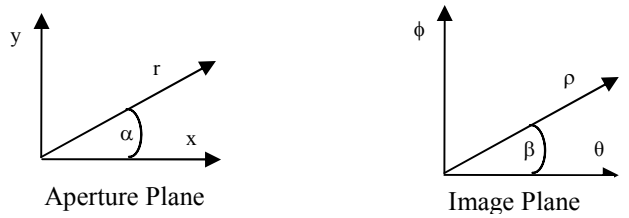

Figure 2.2 Change of Variable for Coordinate Transformation

Making these substitutions into the equation for the total 2-dimensional energy contributions, and noting that the transmission function is independent of α, gives us:

$$U(\rho)\propto\int_{-\infty}^{\infty}\int_{-\infty}^{\infty}T(x,y)e^{ik(x\theta+y\phi)}dxdy=\int_{-\infty}^{\infty}\int_{-\infty}^{\infty}T(r)e^{ik[(r\cos\alpha)(\rho\cos\beta)+(r\sin\alpha)(\rho\sin\beta)]}rdrd\alpha$$

$$U(\rho)\propto\int_{-\infty}^{\infty}\int_{-\infty}^{\infty}T(r)e^{ikr\rho[(\cos\alpha)(\cos\beta)+(\sin\alpha)(\sin\beta)]}rdrd\alpha=\int_{-\infty}^{\infty}\int_{-\infty}^{\infty}T(r)e^{ikr\rho\left[\frac{1}{2}[(\cos(\alpha-\beta)+\cos(\alpha+\beta)]+\frac{1}{2}[(\cos(\alpha-\beta)-(\cos\alpha+\beta)]\right]}rdrd\alpha$$

$$U(\rho)\propto\int_{-\infty}^{\infty}\int_{-\infty}^{\infty}T(r)e^{ikr\rho\cos(\alpha-\beta)}rdrd\alpha$$

To further simplify this equation we make the following substitutions:

$$\chi=k\rho r,\ d\chi=k\rho\,dr \qquad\qquad \eta=\alpha-\beta,\ d\eta=d\alpha$$

Then write the total energy:

$$U(\rho)\propto\int_{-\infty}^{\infty}\int_{-\infty}^{\infty}T(r,\alpha)e^{ikr\rho\cos(\alpha-\beta)}rdrd\alpha=\int_{0}^{\infty}\int_{0}^{2\pi}T(\chi)e^{i\chi\cos(\eta)}\left(\frac{\chi}{k\rho}\right)\left(\frac{d\chi}{k\rho}\right)d\eta=\frac{1}{(k\rho)^2}\int_{0}^{\infty}\int_{0}^{2\pi}T(\chi)\chi e^{i\chi\cos(\eta)}d\chi d\eta$$

$$U(\rho)\propto\frac{1}{(k\rho)^2}\int_{0}^{\infty}\int_{0}^{2\pi}T(\chi)\chi e^{i\chi\cos(\eta)}d\chi d\eta=\frac{1}{(k\rho)^2}\int_{0}^{\infty}T(\chi)\chi\left(2\pi J_0(\chi)\right)d\chi \quad \text{(5, pp. 675, eqn. 11.30c)}$$

To evaluate this integral we employ another Bessel function relationship and integrate both sides with respect to x:

$$\frac{d}{dx}\left[x^nJ_n(x)\right]=x^nJ_{n-1}(x) \qquad \text{(4, pp. 514, eqn. 13.15.1)}$$

$$\int\frac{d}{dx}\left[x^nJ_n(x)\right]dx=\int x^nJ_{n-1}(x)dx \quad\Rightarrow\quad x^nJ_n(x)=\int x^nJ_{n-1}(x)dx\,.$$

Making this Bessel function substitution we can now write the electric field as:

$$U(\rho) \propto \frac{1}{(k\rho)^2}\int_0^{\infty} T(\chi)\chi\left(2\pi J_0(\chi)\right)d\chi = \frac{2\pi}{(k\rho)^2}(\chi)J_1(\chi) = \frac{2\pi}{(k\rho)^2}(k\rho a)J_1(k\rho a) = 2\pi a^2\frac{J_1(k\rho a)}{k\rho a}$$

$$U(\rho) \propto (\pi a^2)\frac{2J_1(k\rho a)}{k\rho a}$$

Absorbing the constants into the normalization factor, I_0, we can now write:

$$I(\rho) = I_U U^2 = I_0\left[\frac{2J_1(k\rho a)}{k\rho a}\right]^2 \qquad \textbf{Eqn. 2.2}$$

This is the function we sought, the normalized intensity distribution at a angle ρ from the central axis on the image plane due to the response of the incoming wave with the aperture plane, and this function is plotted in Fig. 2.3 below. This function is the Point Spread Function (PSF), which gives us the relationship between a point at the aperture plane and the resulting image of this point on the image plane.

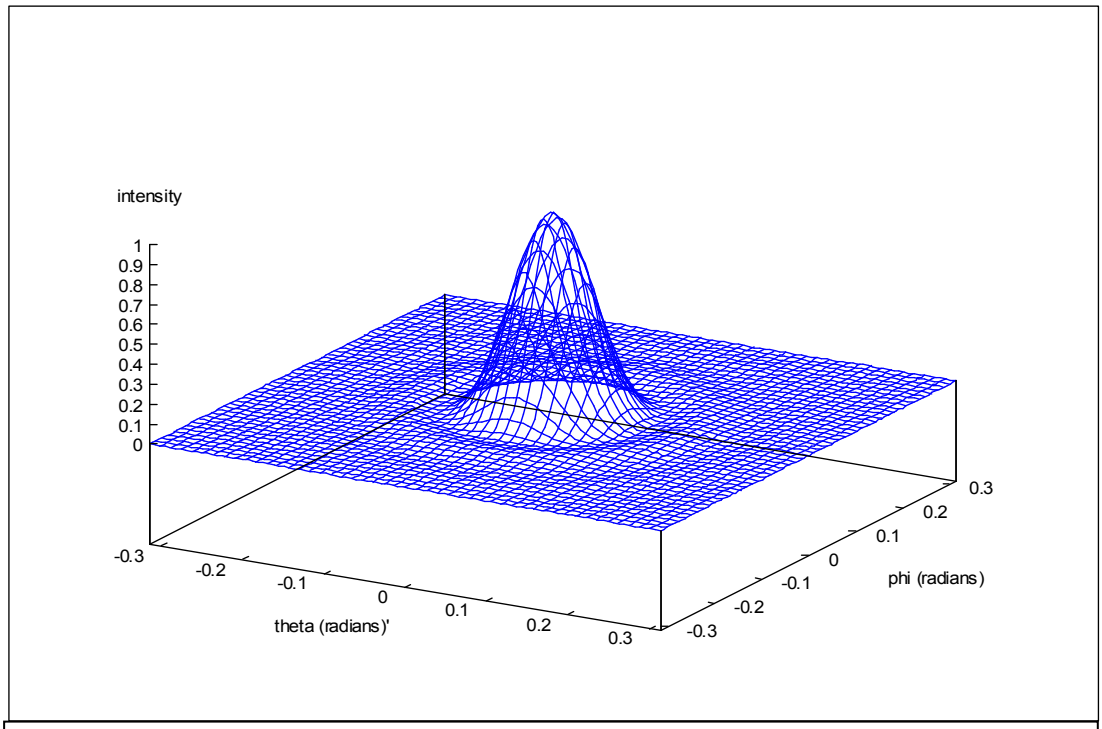

Figure 2.3 Normalized Intensity Distribution for 2-D Circular Aperture

Two Aperture Interference

Now that we've established the PSF for a single aperture, we need the PSF for a pair of apertures. To mathematically model a two element interferometer, separated by a distance D, we convolve the transmission function with the distribution of the apertures. The transmission function is the same as the one used previously:

$$T(r)=\begin{cases}1 & 0\le r\le a\\ 0 & r>a\end{cases}$$

The distribution of the apertures is represented by two delta functions:

$$g(r)=\delta\left(-\frac{D}{2}\right)+\delta\left(\frac{D}{2}\right)$$

The convolution of these two functions is the modified transmission function:

$$M(r)=T(r)*g(r)$$

Previously we sought the Fourier transform of the transmission function, $\mathcal{F}\{T(r)\}=U(\theta)$. We now seek the Fourier transform of the modified transmission function:

$$U_m(\rho)=\mathcal{F}\{M(r)\}=\mathcal{F}\{T(r)*g(r)\}$$

$$U_m(\rho)=\mathcal{F}\{T(r)*g(r)\}=\mathcal{F}\{T(r)\}\,\mathcal{F}\{g(r)\}$$ convolution theorem (5, pp.191, eqn. 34.10)

$$U_m(\rho)=\mathcal{F}\{T(r)\}\,\mathcal{F}\{g(r)\}=U(\rho)\;G(\rho)$$

We next need to find the Fourier transform of the distribution of apertures, $\mathcal{F}\{g(r)\}=G(\rho)$:

$$G(\rho)=\int_0^\infty g(r)e^{ik\rho r}dr=\int_0^\infty\left(\delta\left(\frac{-D}{2}\right)+\delta\left(\frac{D}{2}\right)\right)e^{ik\rho r}dr=\int_0^\infty\delta\left(\frac{-D}{2}\right)e^{ik\rho r}dr+\int_0^\infty\delta\left(\frac{D}{2}\right)e^{ik\rho r}dr$$

$$G(\rho)=e^{ik\rho\frac{-D}{2}}+e^{ik\rho\frac{D}{2}}=2\cos\left(k\rho\frac{D}{2}\right)$$

Using our value for $U(\rho)$ from the previous section (eqn. 2.2), and $G(\rho)$ from above, this leads to:

$$U_m(\rho)=U(\rho)G(\rho)=\left(\frac{2J_1(k\rho a)}{k\rho a}\right)\left(\cos\left(k\rho\frac{D}{2}\right)\right)$$

Which in turn yields a normalized intensity of:

$$I(\rho)=I_0\left(\frac{2J_1(k\rho a)}{k\rho a}\right)^2\cos^2\left(k\rho\frac{D}{2}\right)$$ **Eqn. 2.3**

Examining Fig. 2.4 (below) we can see that the diffraction of a single aperture is now modulated by the influence of the second aperture. This modulation of the intensity distribution results in bands of light and dark areas (the maxima and minima of the intensity) and are referred to as fringes. For a single aperture the incoming wave undergoes diffraction and the bands are referred to as diffraction fringes,

whereas the aperture pair also undergoes interference producing interference fringes. The diffraction fringes form the envelope of the interference fringes (see Fig. 2.4 below), and it's the presence of these interference fringes that we can exploit to increase the resolving power of an optical system. Now that we have derived the PSF, for both a single aperture and a pair of apertures, we have the tools for analyzing the resolving power of an aperture pair and compare it with the resolving power of a single aperture.

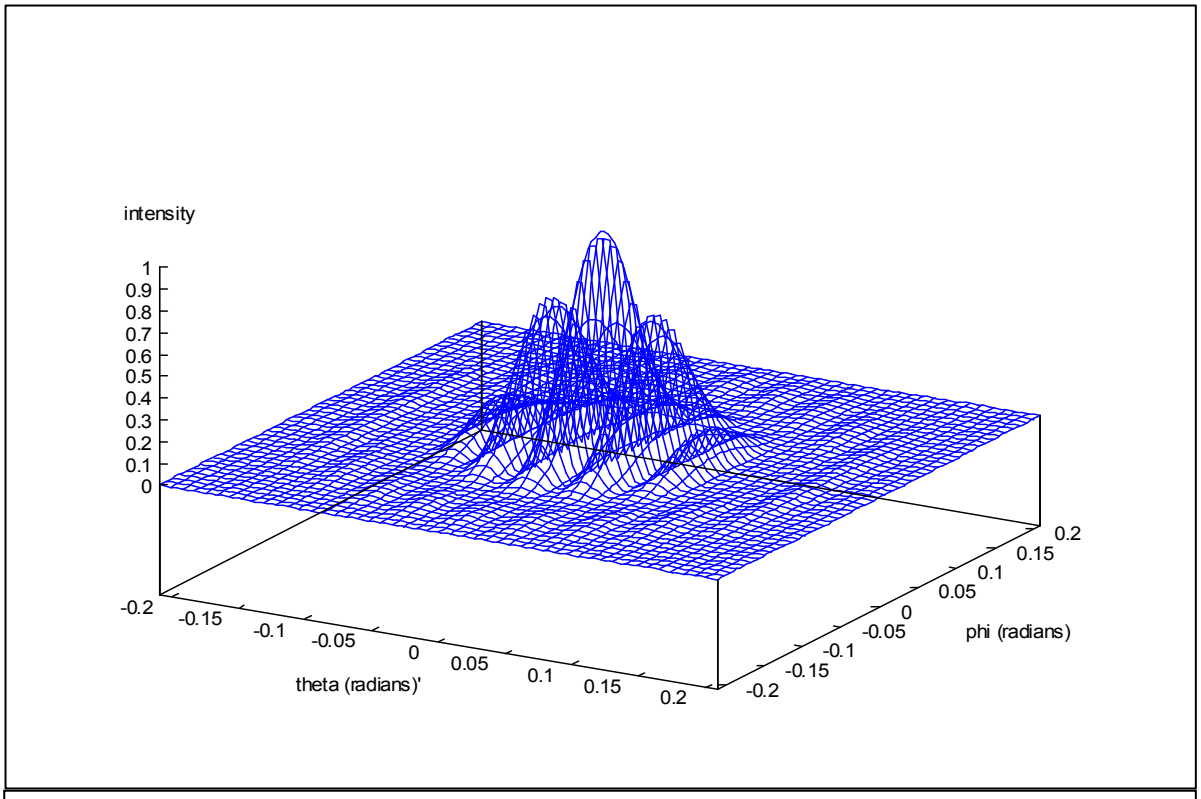

Figure 2.4 Modulated Intensity Distribution due to Interference Effects from 2nd Aperture

Resolution

The resolving power of a telescope is often given in terms of the minimum angular separation between two sources that is required to determine that there are two sources. Raleigh's criterion (11, pp.938) establishes that two sources are considered resolved when the central maxima of one source coincides the first minima of the second source. This is illustrated above in Fig. 2.5 (below), where the angular distance ρ is measured in degrees. Relative to the source represented by the blue curve, the red source is considered unresolved while the green source is just at the threshold of Raleigh's criterion and is considered barely resolved.

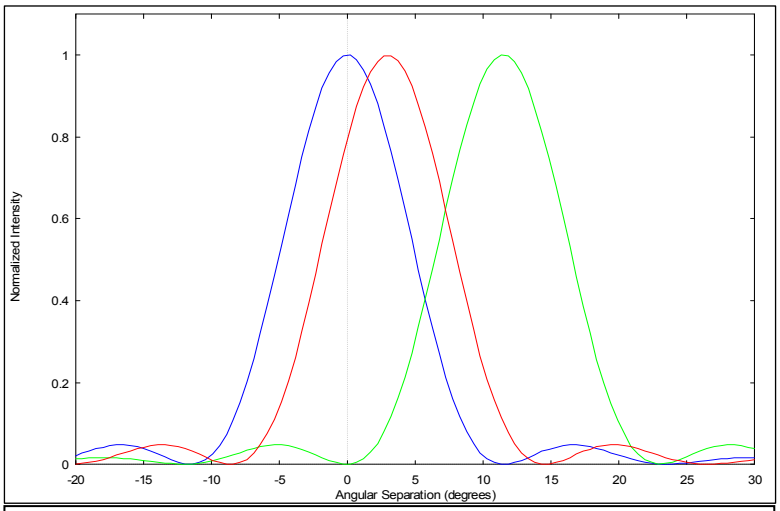

Figure 2.5 Raleigh's Criterion

The angular distance between the central maxima and the first minima of the intensity function is called the critical angle. This angle can be obtained by finding the zeros of the intensity function,

$$I(\rho) = I_0\left[\frac{2J_1(k\rho a)}{k\rho a}\right]^2.$$

Although the value of $J_1(0) = 0$ we find that:

$$\lim_{x\to 0}\frac{J_1(k\rho a)}{k\rho a} = 1$$

and hence $k\rho a$=0 is not the first zero of the intensity function. The next zero is found from interpolating from a table of Bessel functions (6, pp.248, Table 15), and this occurs at $k\rho a$=3.88. We can insert this value into the argument of the Bessel function and solve for the critical angle (measured in radians):

$$k\rho_c a = 3.88 \quad \Rightarrow \quad \left(\frac{2\pi}{\lambda}\right)\rho_c a = 3.88 \quad \Rightarrow \quad \rho_c = \frac{3.88\,\lambda}{2\pi a} \approx \frac{1.22\,\lambda}{2a} \qquad \textbf{Eqn. 2.4}$$

Where a is the radius of the aperture and λ is the wavelength of the observed light. It should be noted that the resulting image has large a percentage of the overall intensity inside a disk with a radius equal to the critical angle, and this disk is known as the Airy disk. Next we examine how these results relate to the resolving power of 3 specific aperture configurations, a 0.25m aperture, a 10m aperture, and that of a pair of 0.25m apertures separated by 10m.

Assuming we are observing at 550nm (approximately the center of the visible spectrum), we can place this value into the results from above, and along with our aperture diameters we have:

Case 1: (single 0.25m aperture) $$\rho_c = \frac{1.22\lambda}{2a} = \frac{1.22(550\times10^{-9})}{2a} = \frac{6.71\times10^{-7}}{0.25} = 2.68\times10^{-6}\,\text{rad.}$$

Case 2: (single 10m aperture) $$\rho_c = \frac{1.22\lambda}{2a} = \frac{6.71\times10^{-7}}{10} = 6.71\times10^{-8}\,\text{rad.}$$

For the third case we are looking for the first zero of the PSF of last section:

$$I(\rho) = I_0\left(\frac{2J_1(k\rho a)}{k\rho a}\right)^2 \cos^2\left(k\rho\frac{D}{2}\right)$$

We use the results from above for the first argument in the Bessel function, and need to find the first zero of the cosine argument. This occurs when the argument of the cosine function is equal to π/2:

$$\frac{k\rho D}{2} = \frac{\pi}{2} \Rightarrow k\rho D = \pi \Rightarrow \frac{2\pi}{\lambda}\rho D = \pi \Rightarrow \rho = \frac{\lambda}{2D}$$

Before proceeding, we should note that we just need either term in the PSF to equal zero and the entire function equals zero. The cosine function will clearly dominate and we need only concern ourselves with that term to find the critical angle:

Case 3: (pair 0.25m aperture) $$\rho_c = \frac{\lambda}{2D} = \frac{550\times10^{-9}}{20} = 2.75\times10^{-8}\,\text{rad.}$$

Converting these results into units of arcseconds we have:

Case 1) 2.68×10^{-6} rad.=0.55arcs

Case 2) 6.71×10^{-8} rad.=0.014arcs

Case 3) 2.75×10^{-8} rad.=0.0057arcs

The PSF for each of these apertures are plotted in figures 2.6, 2.7, and 2.8 respectively (at the end of this section).

From these results we can conclude that the critical angle is significantly reduced with both increasing the aperture radius and increasing the distance between apertures. If we examine the graph of the PSF for case 1 and case 3 (figures 2.9 and 2.10 respectively, at the end of this section) we see that the diffraction envelope is dictated by the radius of the aperture, and symmetrical about the central axis of the image plane. Examining Fig. 2.11 reveals, with the aid of significant scaling on the θ-axis, the degree of

interference induced upon the diffraction envelope due to the effect of the aperture pair, while the distance between fringes is affected by the spacing between the apertures. This establishes some of the principals behind a basic interferometer and how the aperture diameter and the aperture separation relate to each other and the resulting PSF. The next step is to consider how the fruition of this theory is being applied in some of the currently operating astronomical optical interferometers.

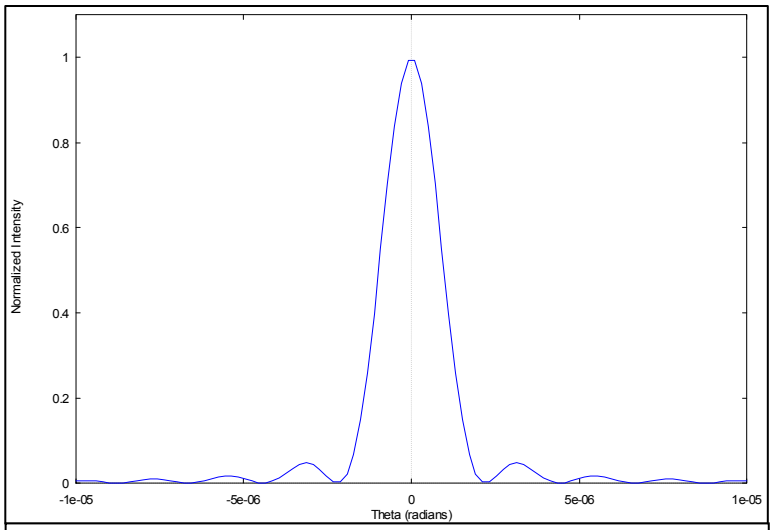

Figure 2.6 1-D Intensity Distribution of a 0.25m Aperture

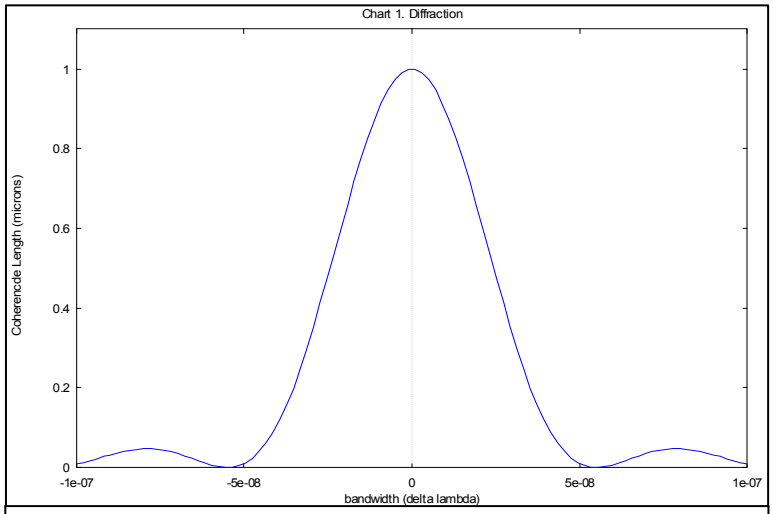

Figure 2.7 1-D Intensity Distribution of a 10-meter Aperture

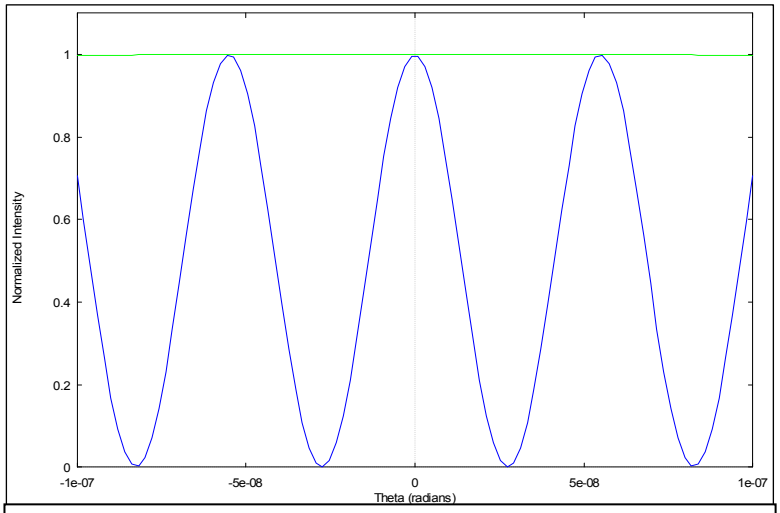

Figure 2.8 Intensity Distribution of a Pair of 0.25m Apertures

Note: Figures 2.9, 2.10, and 2.11 are plots of the polar function projected onto the Cartesian image plane.

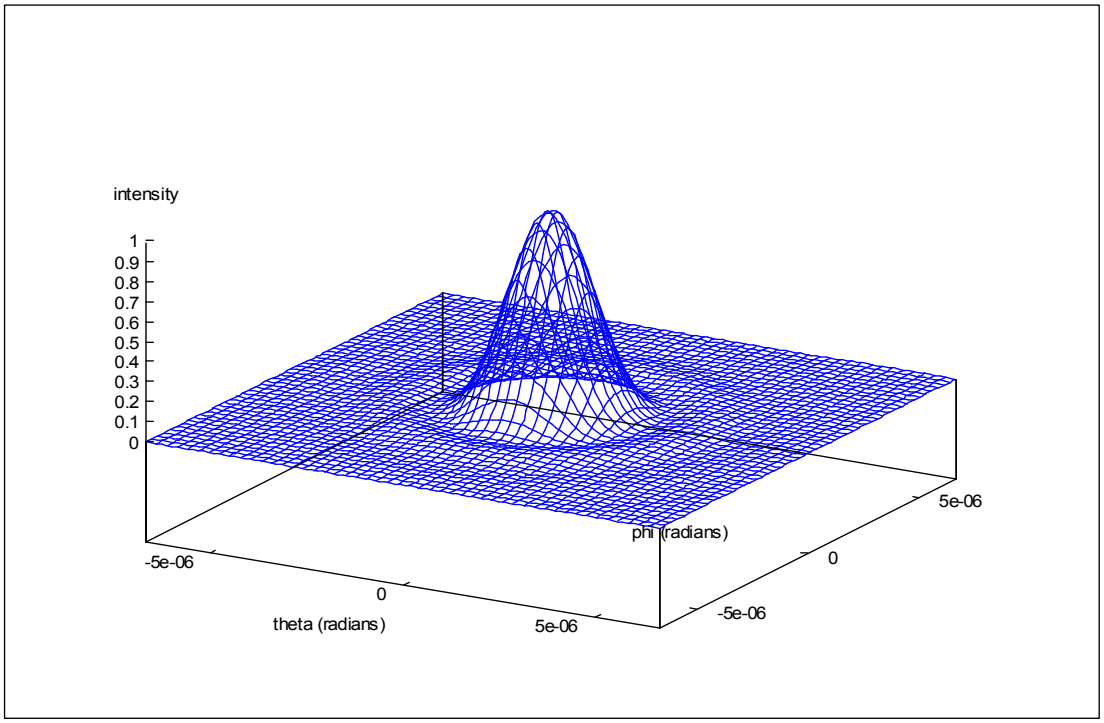

Figure 2.9Intensity Distribution of a 0.25m Aperture

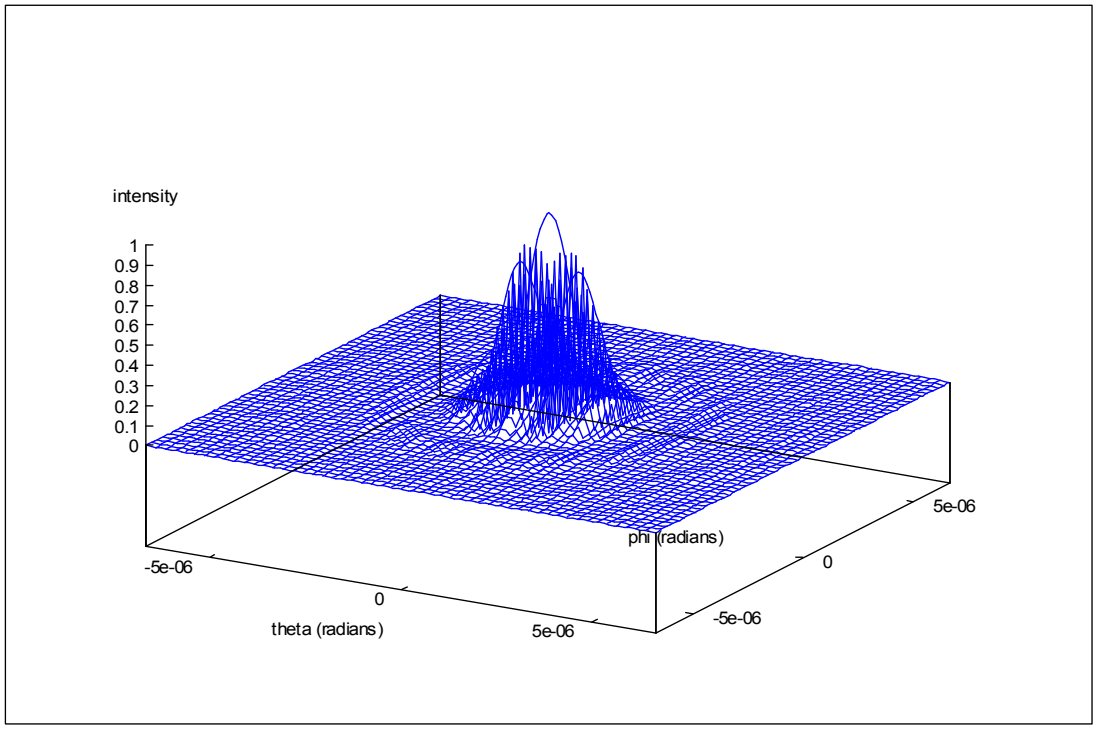

Figure 2.10Intensity Distribution of a pair of 0.25m Apertures with 10m Separation.

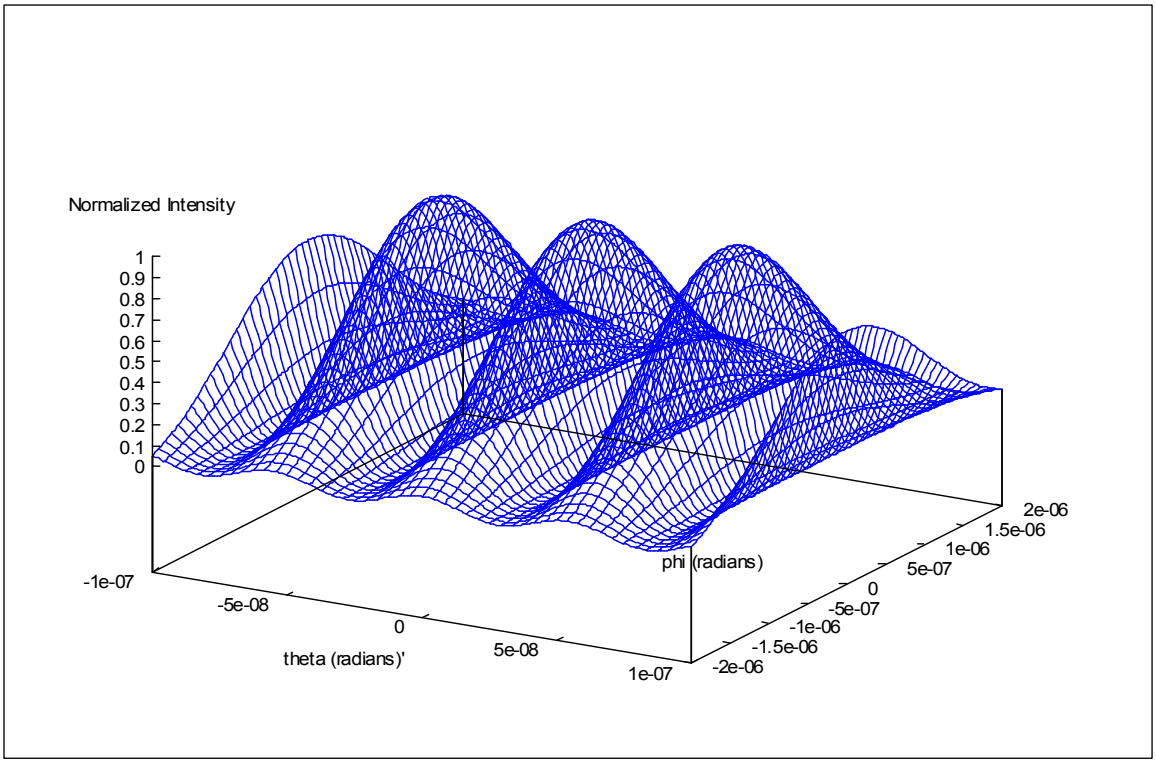

Figure 2.11 High Resolution Modulated Intensity Distribution of Aperture Pair

III Instrument Measurements and Design Considerations

In this chapter we will examine what an astronomical interferometer measures and how the configuration of the array affects these measurements, in particular the orientation of the apertures with respect to the target object. Our objective will be to identify aspects of an array that can be controlled with careful design consideration. But before doing this we will examine what a typical astronomical interferometer measures.

Visibility

In the previous section we examined the simplest case of interferometry, though in practice the construction of an image generally requires a composite of many measurements. Previously we defined the source to be a point source of a given wavelength and plotted (Fig. 2.9) the Fourier transform of that source. In practice we can map intensity measurements at various points of the distribution of the Fourier transform of the source, and with sufficient data points inversion algorithms can be employed to reconstruct an image of the source. For instance, previously we found the Fourier transform of a point source generates a Gaussian distribution, therefore a plot of intensities measurements with a Gaussian distribution will produce a point source for a final image after inversion.

These measurements are referred to as visibility measurements. Let's consider a simple two-aperture interferometer such as the one illustrated in Fig. 3.1 below (adapted directly from Von Der Luhe, et. al.).

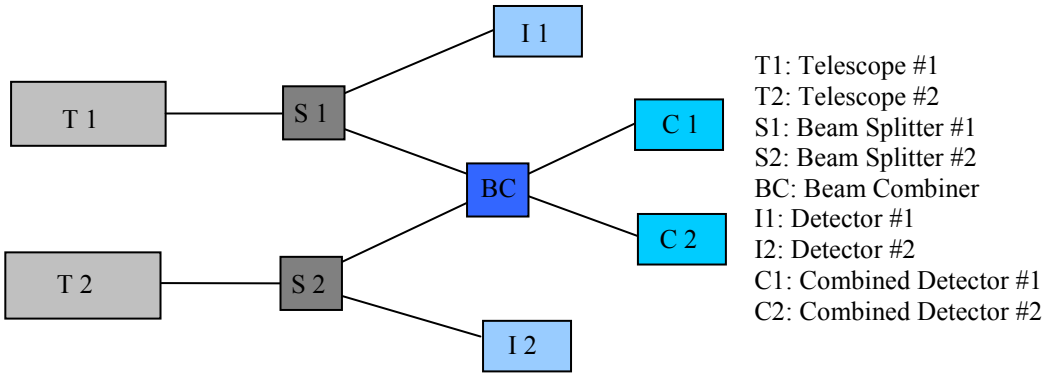

Figure 3.1 Schematic of Simplified Interferometer

This arrangement consists of two telescopes (T1 and T2), each of which feeds into a beam splitter (S1 and S2). The outputs from the beam splitter direct part of the beam to a detector (I1 and I2) and the other part to the beam combiner (BC). The beam combiner mixes the incoming beams and produces two output beams that are directed to detectors (C1 and C2). This arrangement employs Michelson (or pupil-plane) combination, rather than Fizeau (or image-plane) combination, where the energy transmitted or reflected at the beam combiner depends upon the phase relationship of the incoming waves. The intensity of the

beam is then measured at each of the detectors, and from these values the visibility, V, is calculated as follows:

$$V\cos(\phi)=\frac{C_1-C_2}{4\sqrt{I_1 I_2}}$$ (ϕ = phase between beams) (8, pp. 91, eqn.12)

This gives the relationship between the individual intensities and the combined intensities, and is the quantity generally measured in optical interferometry.

This measurement gives the value of the visibility at a given point in the UV-plane. The UV-plane is a map of the square of the visibility, or the intensity, distribution (see Fig. 2.10), and in practice a number of visibility measurements are taken at different points on this plane. The image is extrapolated through various techniques and algorithms to fill in the missing points on the UV-plane. There are various methods for collecting data at these various points, as well as several restrictions. Much of this is dependant upon the configuration of the interferometer, as we shall see the following section.

Baselines and Optical Path Length

The exact design of the interferometer will dictate the coverage of the UV-plane possible with a given instrument. As an example, the Keck Interferometer (KI) consists of two independently mounted telescopes, with apertures of 10m and a baseline of 84m. A sample mapping of the UV-plane that can be covered with instrument is shown below in Fig. 3.2.

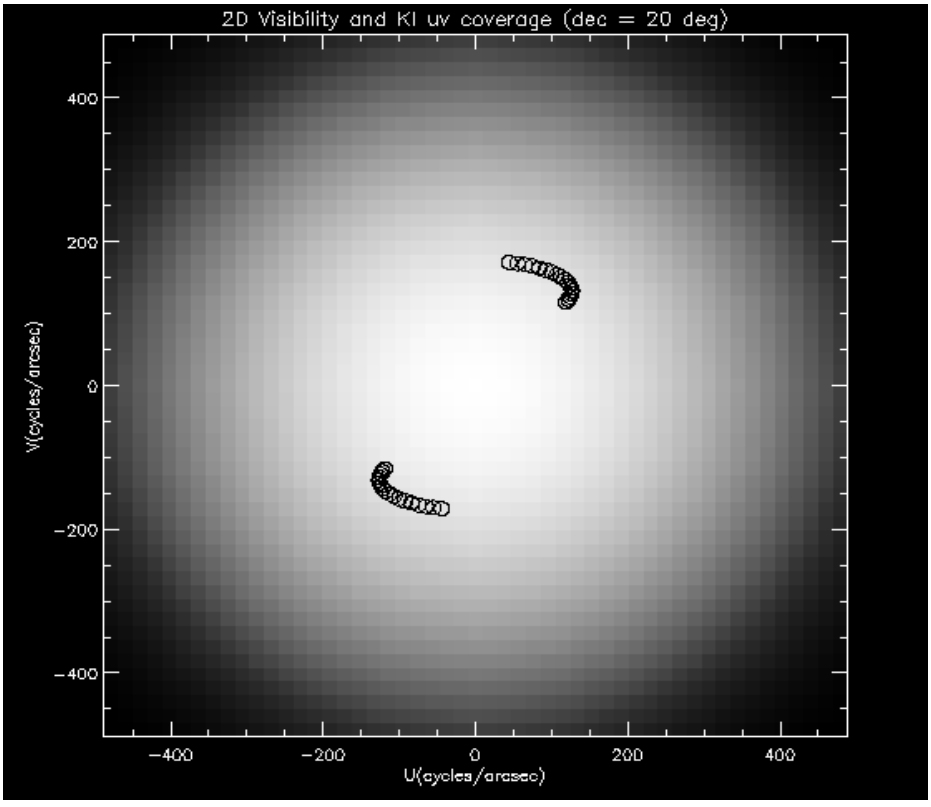

Figure 3.2. The 2D visibility (squared) map of the Gaussian brightness. The superposed arcs show a realistic KI sampling of spatial frequencies. (7)

The first thing to note is that the coverage of the plane is rather limited. The samplings are based on the estimated number of measurements possible during a given observing session. A longer observing session would allowing more data points to be gathered, as would shortening the integration time between detector readouts. The location on the plane is determined primarily by the baseline of the interferometer and the diameter of the apertures. The data points map out an oval, where the major axis is determined by the diameter of the aperture, and the minor axis is determined by the baseline of the interferometer, as we determined at the end of the previous chapter. And one last point to note is the orientation of the ellipse with the UV-plane. This orientation is determined by several factors, among these are the position of the target on the celestial sphere and the orientation of the interferometer baseline relative to the celestial sphere.

If the celestial sphere were static, measurements would be redundant, but due to the rotation of the Earth the orientation of the baseline with respect to the celestial sphere is changing with time (or field rotation). While the effective length of the baseline of the interferometer changes in time due to the motion telescope as it tracks the target. The source of this baseline variation can be seen from Fig. 3.3 below, the effective baseline is the baseline projected onto the incoming wavefront and is referred to as the projected baseline. These are the two primary factors that allow for measurements to be taken at different locations on the UV-plane with KI. We can see that the orientation of the baseline, the diameter of the apertures, and the length of the baseline are all parameters that we would like to vary in order to enhance the UV-plane coverage.

Another thing to note is that the diameter of the circles indicating data points in Fig. 3.2 are determined by the integration times and the motion of the celestial sphere. The measurement is an average visibility over the approximate area of the circle. Again this is basically field rotation, and being able to control field rotation would allow for much greater integration time and enhanced resolution. This effectively reduces the area over which the average is taken.

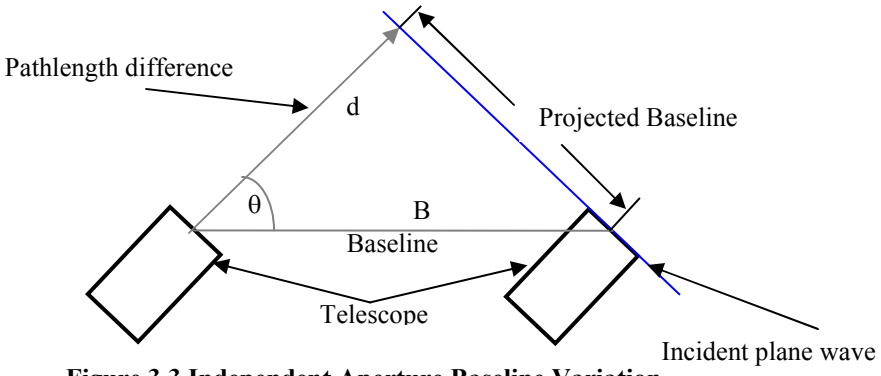

Figure 3.3 Independent Aperture Baseline Variation

Another effect to consider with independently mounted apertures is an inherent pathlength difference that also varies with time. In Fig. 3.3 (above), we can see that the distance d will change with the position the telescopes. Compensation must be made in the optical pathway to counteract this pathlength difference, and is generally done with delay lines consisting of a series of mirrors whose positions change in time as well. This is known as optical pathway delay (OPD). A second reason for varying the optical pathlength is to perform fringe shifting. In practice, fringe shifting is performed by varying the pathlength and measuring the intensity at various points.

Often the large scale and the small scale OPD can be handled independently. Large scale OPD is extremely complicated, bulky, sensitive, and technically demanding. Small scale OPD can be handled with a minimum of complication and expense, and with a wide range methods. Therefore we wish to dispense with the large scale OPD, which is possible with a short baseline instrument, but the small scale OPD is imperative and should be as functionally robust as feasible.

Design Considerations

At this point we can summarize the major design considerations for the proposed interferometer prototype.

- Variable baseline length
- Variable baseline orientation
- Variable aperture diameter
- Multiple apertures
- Field rotation control
- High-precision small scale OPD control

The incorporation of these features into the proposed interferometer design will allow for very precise measurements with excellent UV-plane resolution. How this is accomplished deserves a closer look, and an overview of the proposed interferometer design is in order.

IV Proposed Design Overview

In this chapter we will examine the overall basic design of the proposed prototype optical interferometer array, which consists of three major systems (illustrated below in Fig. 4.1):

- Array Mount and Drive
- Array Platform and Drive
- Optical System

The array platform and drive provides the support and positioning of the optical system. The optical system consists of the actual telescopes and the optical pathways to the detectors. We will examine both of these systems more closely, but first we'll consider the array mount and drive which supports and positions the array platform.

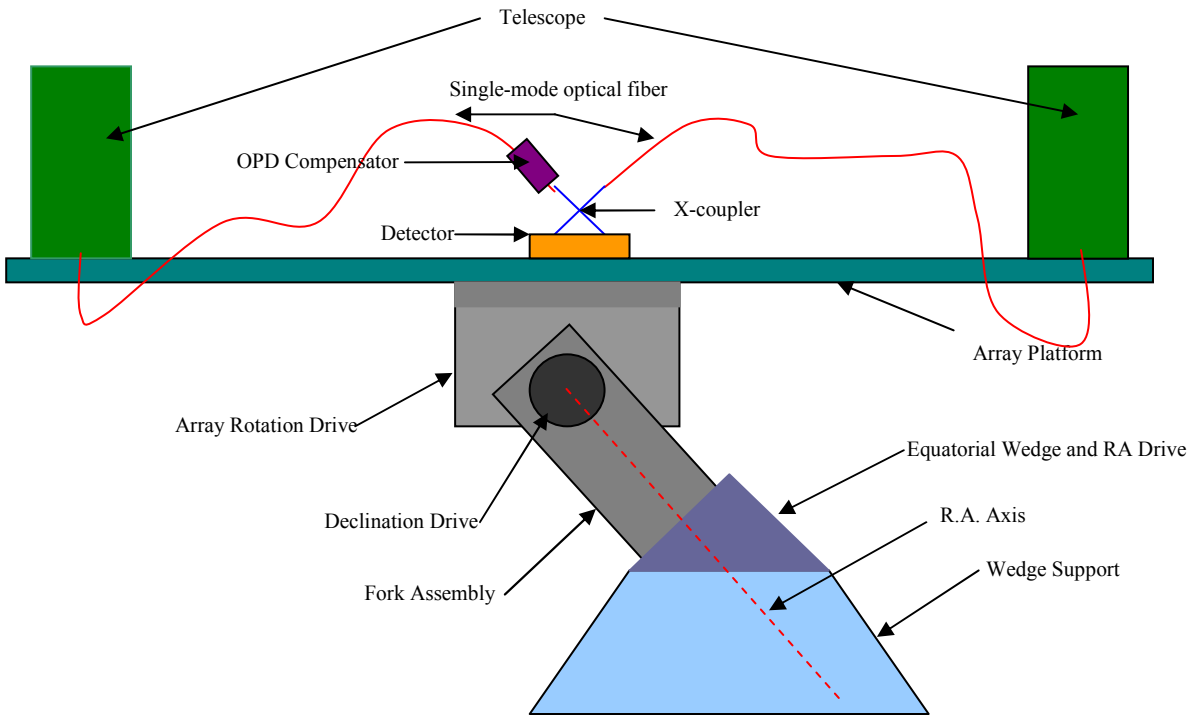

Figure 4.1 Interferometer Overview

Array Mount and Drive

This is perhaps the simplest of the major systems, and the preferred mount is a polar mount. This type of a mount allows for high precision tracking and eliminates all field rotation in the telescopes themselves, as well as field rotation of the baseline as well. In particular, a forked-polar mount provides the greatest flexibility (see Fig.e 4.1 above). A typical configuration includes a robust base that acts as a support for the equatorial wedge. The angle of this wedge is such that the R.A. axis is aligned to coincide

with the polar axis. This wedge supports the fork assembly that houses the declination drives, which in turn supports the array drive assembly.

Once adjustments are made to the right ascension and declination, the central axis of the array platform should be aligned with the target object. In order to track the object a rotation about the R.A. axis is required while holding the declination axis fixed. This geometry allows the array baseline orientation to remain fixed relative to the target object for longer exposure times and signal integration.

For more robust versions of the array platform and instruments, or due to location of the observing site, the polar mount may be unsuitable. In these situations an alt-azimuth mount would suffice but field rotation would be inherent with this type of mount. The array platform and drive assembly can compensate for this and a closer look at this system is now in order.

Array Platform and Drive

The array platform supports the optical system and positions the telescopes within the array, while the drive assembly allows rotations about the central axis of the array platform for baseline orientation positioning. In Fig. 4.2 a plan view (top) and an elevation view (bottom) of the array platform illustrate the basic components of the assembly.

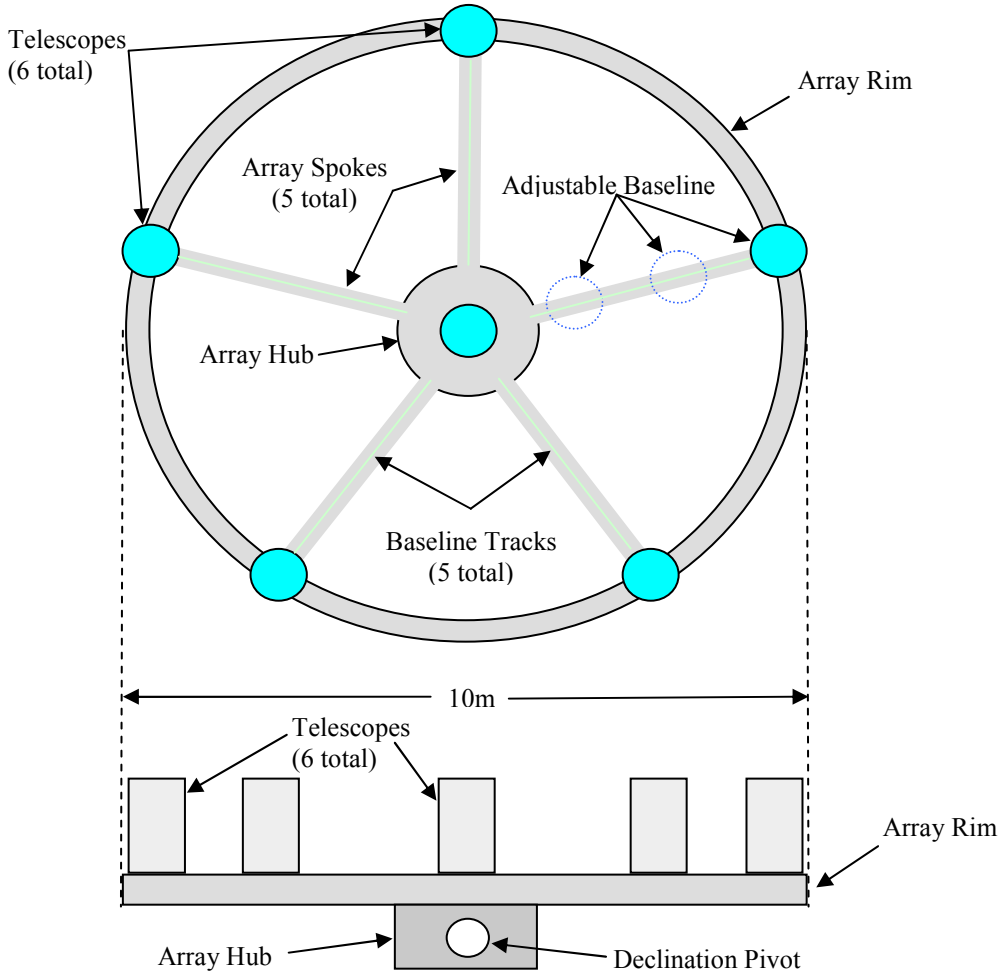

Figure 4.2. Plan View and Elevation View of Array Platform.

The platform consists of a central hub connected to a perimeter rim via 5 spokes. Baseline tracks are placed upon each of these spokes and five of the telescopes can be positioned along the tracks for variable baseline lengths, while the sixth telescope remains fixed at all times. This arrangement allows for complete pairing of all telescopes forming 3 independent baselines at any given time. The total number of independent baselines, B, for an array consisting of N telescopes is B=N(N-1)/2 (8, pg. 986), so for a six telescope array there are 15 independent baselines.

That is, there are 15 independent baselines for a particular baseline length and for a particular orientation of the array platform relative to the celestial sphere. Reconfiguring either of these parameters provides another 15 independent baselines and visibility measurements. This is where the versatility of this instrument is most pronounced. In order to position an arbitrary baseline orientation of the interferometer a rotation of no more than about 72 degrees, or one-fifth of a revolution, is required. The relative potential UV-plane coverage is illustrated in Fig. 4.3 below. The grey doughnut shaped area represents the potential coverage of the proposed array and the blue ellipse represents some arbitrary potential coverage for a fixed orientation. The length of the minor axis of the ellipse increases with decreasing baseline length, therefore the longest baseline of the array determines the minimum length of the minor axis. The aperture diameter determines length of the major axis and increases with decreasing aperture diameter, employing aperture stops allows one to increase the axis length as required.

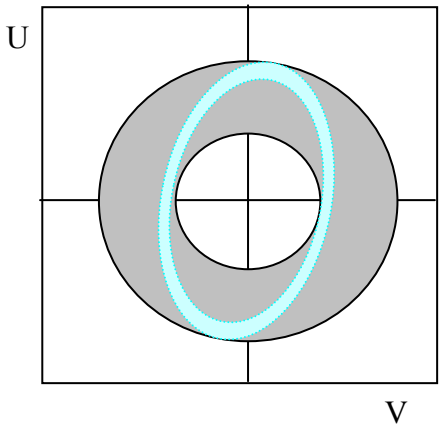

Figure 4.3 Relative UV-Plane Coverage

Positioning, tracking, and error corrections are easily achieved through a number of different means, though in general the gearing and motors for such applications are widely commercially available. The major structural elements of the platform will need detailed mechanical engineering and custom fabrication for more demanding instruments. This same basic design can be scaled down in many ways for less demanding or amateur applications, and decrease costs substantially. The optical system that is supported by the array platform now deserves a more detailed inspection.

Optical System

This design allows for a wide range of telescopes to be coupled with the array platform. Though the specific choice of aperture diameter will have a direct impact on cost of not only the telescopes themselves, but also on the structural robustness of the array platform and mount as well. The most important factor in general would be that the telescopes are well matched in characteristics such as mirror quality, geometry, focal length, etc. For smaller apertures there are a number of excellent suppliers of high quality telescopes, but as the aperture diameter increases so does the need for custom fabrication. As far as wavefront correction is concerned there are commercially available Adaptive Optics (AO) systems suitable for many applications, but again for more demanding specifications custom design and fabrication may be required.

Guiding the incoming wavefront from the telescope to the beam combiner can be achieved with single mode fiber optics (SMFO) (14). Fiber optics have been employed in such applications for more than a decade, including instruments used in the Sloan Digital Sky Survey (10, pp.92), and the characteristics and quality of fiber optics can be easily controlled for the most demanding needs at a very low cost. Polarization-preserving SMFO's have a high birefringence, which dominates over any random birefringence, while maintaining a well defined principle axis of polarization (12, pp. 312). In addition, SFMO's provide modal and spatial filtering: "Whatever the injection conditions at the input, the output beam is perfectly stable and coherent, since its profile is determined by the waveguide structure. All phase perturbations in the pupil, whether they are static (optical aberrations) or dynamic (induced by turbulence), are removed by the coupling process, and the injected starlight may vary in intensity only." (12, pp. 313) The positioning of the fibers at the exit pupil can be achieved by mounting the end of the fiber to a fixed block as was done with the SDS survey (10, pp.93) or with the use of micropositioners (13, pp.9). It should be noted that there is inherent signal loss (27, pp. 255) as the wavefront propagates through the fiber and at each fiber interface, and therefore places certain limits on the length one can effectively employ. In these cases collimating lens and mirrors can be used to direct the wavefront and minimize signal loss. Avoiding the use of conventional optics drastically reduces construction and maintenance costs, as well as reduces instrument calibration during the observing session.

The coupling fibers from the telescopes feed into a Y-coupler that allow the signal to be split and feed the intensity detector and the beam combiner (see Fig. 3.1 above). In order to accommodate multiple baseline pairings, the feed leading to the beam combiner will need to be redirected to a switching mechanism such as a photonic switch. Unlike most optical switches, photonic switches preserve all of the characteristics of the incoming signal. Generally there are two types, with some hybrids, of photonic switches: fiber positioning and reflective positioning. Fiber positioning utilizes stepper motors to reposition the end of the input fiber to mate up with the end of the desired output fiber. Reflective

positioning generally employs micro-prisms and/or micro-mirrors do direct the input signal to the desired output fiber. These switches allow for rapid reconfiguration of the array pairing, are very reliable, and are very efficient. State of the art telecommunications equipment is commercially available for a competitive price from a wide range of manufacturers, and would be ideal for most applications.

The output from the switch would then be directed to the beam combiner, and in this case employing another fiber optic component would be more than adequate for all but the most demanding applications. X-couplers are available in a wide range of configurations, specifications, and mixing ratios (12, pp. 313). Simple, yet highly efficient, versions are little more than a pair of optical fibers twisted and fused together. These outputs are then in turn directed to the detector or other instruments. With an optical interferometer the signal strength is generally very weak and losses due to transmission along the optical pathway must be minimized. Current fiber optics, couplers, and switches are extremely efficient and introduce minimal signal loss along the length and at the interfaces, making them idea for this application. In addition, Integrated Optics may soon become commercially available and suitable for optical interferometers, which would allow direct coupling of the optical fiber to the chip and all switching can be handled internally (9).

Finally the last design consideration to be addressed is the short scale OPD. Through the use of piezoelectric ceramics the optical fibers can be stretched to vary the optical path length in a very controlled way (12, pp. 313). This allows for compensation in the optical pathway to variations in optical fiber length, positioning, etc., as well as allowing the path length to be varied for fringe scanning.

Cost Effectiveness

Now that the basic design has been laid out, an estimate for a specific example can be put forth, and we will consider an array with a diameter of 10ft. and employing 16in. diameter objectives. Such instruments can be purchased off the shelf and weigh under 100lbs. each, so with six telescopes the total load due to instruments on the platform will be under 600lbs. Using a pentagonal rim, rather than a circular one, of steel construction, along with steel spokes and a steel hub. Comparing this cost (see table 4.1 below) with the price of a 50" Dobsonian reflector telescope at $122,000 (Orion Telescopes, Watsonville, Ca.) the cost effectiveness of the design is clear. With no drive mechanisms the Dobsonian is useless for anything other than visual observing, while the proposed instrument is capable of conducting cutting edge research.

Table 4.1 Estimated cost of 10ft. Diameter Array w/16" Apertures

ITEM		Unit Price	Total Cost
Telescopes	6 16" apertures	$7,500.00	$45,000.00
Adaptive Optics	6 NT67-102	$10,000.00	$60,000.00
F.O. Adapters	6 Fiber Optic Positioner	$1,200.00	$7,200.00
Platform	Rim, Spokes, Hub		$35,000.00
Platform Drive	Drive and Housing		$20,000.00
Spoke Rails/Drives		$2,200.00	$11,000.00
Mount	Fork, Bearings, Drives, Etc.		$30,000.00
Base	Footing and Pedestal		$30,000.00
Fiber Optic Cables			$1,500.00
F.O. Couplers			$1,500.00
Photonic Switch			$5,500.00
F.O. Fabrication			$3,500.00
OPD Compensator		$1,200.00	$7,200.00
		Total	**$257,400.00**

This covers an overview of the proposed prototype design of the interferometer. The objectives laid out previously for design considerations have all been addressed and incorporated into the proposed design. There are many modifications that can be made to accommodate the needs of the particular user and their budget, as well as several enhancements that could be incorporated to boost performance. This basic design can be scaled to meet the needs of the amateur, and professional as well. Although such an instrument can never rival the resolution of long baseline interferometers, it is conceivable to construct fairly large arrays with platform diameters of 15-20 meters, or more. Larger instruments such as these could easily incorporate additional spokes in the platform for enhanced baseline coverage.

Bibliography and References

1) Haniff, Chris A. "High Angular Resolution Astronomy on a Shoestring." Fiber Optics in Astronomy III. Astronomical Society of the Pacific. San Francisco. 1998.

2) Charbonneau, et. al. "Detection of an Extrasolar Planet Atmosphere." The Astrophysical Journal, 568:377-384. March 20, 2002.

3) Griffiths, David. Introduction to Electrodynamics. Prentice-Hall Inc. New Jersey. 1999.

4) Boas, Mary. Mathematical Methods in the Physical Sciences, 2nd ed. John Wiley and Sons. New York. 1983.

5) Spiegel, M. Liu, J. Mathematical Handbook of Formulas and Tables, 2nd ed. MacGraw-Hill. New York. 1999.

6) Arribas, Mediavilla, Watson. Fiber Optics in Astronomy III. Astronomical Society of the Pacific. San Francisco. 1998.

7) Millan-Gabet, Rafael. April 09 2005. http://nexsci.caltech.edu/software/KISupport/v2tutorial.html

8) Von Der Luhe, Oscar. Ageorges, Nancy. "Imaging in Interferometry." High Angular Resolution in Astrophysics. Kluwer Academic Publishers. Boston. 1997.

9) Berger, Jean Philippe. et. al. "Combining Up To Eight Telescope Beams In A Single Chip." Interferometry In Optical Astronomy. The International Society For Optical Engineering. USA. 2000.

10) Seigmund, Walter A., et. al. "Performance of the Fiber-Positioning System for the Sloan Digital Sky Survey." Fiber Optics in Astronomy III. Astronomical Society of the Pacific. San Francisco. 1998.

11) Halliday, Resnick, and Walker. Fundementals of Physics, 5th Ed. John Wiley & Sons, inc. 1997.

12) Coude du Foresto, V. "Optical Fibers in Astronomical Interferometry." Fiber Optics in Astronomy III. Astronomical Society of the Pacific. San Francisco. 1998.

13) Parry, Ian R. "The Astronomical Uses of Optical Fibers." Fiber Optics in Astronomy III. Astronomical Society of the Pacific. San Francisco. 1998.

14) Tuttle, Carl E. Prasad, Sudhakar. "Field Correlation Effects in Multiple-Core Fibers for an Optical Imaging Interferometer." Fiber Optics in Astronomy III. Astronomical Society of the Pacific. San Francisco. 1998.

15) Berger, J. P. "Guided Optics in Interferometry." Interferometry for Optical Astronomy II. Society for Photo-Optical Instrumentation Engineers. USA. 2003.